Disclinations in C_{60} molecular layers on WO_2/W(110) surfaces

S. I. Bozhko,[1,2] V. Taupin,[3] M. Lebyodkin,[3] C. Fressengeas,[3] E. A. Levchenko,[4] K. Radikan,[2] O. Lübben,[2]
V. N. Semenov,[1] and I. V. Shvets[2]

[1]*Institute of Solid State Physics, Russian Academy of Science, 142432 Chernogolovka, Moscow District, Russia*
[2]*Centre for Research on Adaptative Nanostructures and Nanodevices (CRANN), School of Physics, Trinity College Dublin, Dublin 2, Ireland*
[3]*Laboratoire d'Etude des Microstructures et de Mécanique des Matériaux, Université de Lorraine/CNRS,*
Ile du Saulcy, 57045 Metz Cedex, France
[4]*Department of Physics, Astrakhan State University, Astrakhan 414056, Russia*

A scanning tunneling microscopy study of a planar close-packed C_{60} hexagonal molecular layer on a WO_2/W(110) substrate reveals the existence of C_{60} domains exhibiting two preferred orientations at an angle with an underlying periodic groove structure in the substrate. An analysis of the van der Waals interactions between substrate and layer retrieves the observed misorientations as those corresponding to minima in the interaction energy of the substrate-layer system. The misorientation between two C_{60} domains is accommodated in a tilt boundary by a linear array of molecular structural units identified as disclination dipoles, i.e., rotational defects in the hexagonal structure of the layer. A field theory of disclinations and dislocations is used to construct maps of the elastic energy, strains, curvatures, and stresses induced by the lattice defects over the layer. The predicted regions of high compression are found to overlap with those where the fullerene molecules do not undergo rotation.

PACS number(s): 61.72.Lk, 61.72.Mm, 68.55.ap

I. INTRODUCTION

Research for molecular electronic devices not based on the paradigms of conventional silicon is currently in full swing. Fullerenes have attracted considerable attention in recent years due to their potential in surface chemistry and nanotemplating [1,2], nonlinear optics [2,3], single-molecule transistors [4,5], and especially molecular electronics, because of their tunable electronic properties resulting in superconducting or semiconducting behavior [4,6,7]. C_{60} molecules arranged in planar structures are considered as good candidates for the development of such devices. Close-packed C_{60}(111) molecular layer films with low defect occurrence and ultimate areal densities of the order of 10^{14} mol/cm^2 are of particular interest in this respect. Formation of islands of well-ordered close-packed hexagonal one-molecule-thick layers were reported on various substrates including metals [8], semiconductors [9], oxides [10,11], and substrates covered by buffer layers [12,13], which suggests the presence of strong intermolecular interactions. However, the C_{60}-substrate interactions may also influence properties of the layers such as the shape and the orientation of the islands [10,14,15]. Thus, the structure of the C_{60} layers is determined by a competition between planar C_{60}-C_{60} and substrate-layer interactions.

Only a few articles have been dealing with the microstructure of defects in planar hexagonal C_{60} layers. In [13,16], it was established that large arrays of these layers usually contain point defects. The layers can also include regions with different crystallographic orientations separated by disordered regions, or even coherent twin boundaries [17]. Additional structuring can be observed at low temperature, when the rotation of C_{60} molecules is suppressed, i.e., when the molecules are not only representative of a lattice location in the crystallographic structure, but are also characterized by their own orientation. In this case, the two-dimensional C_{60} layer can feature distinct domains where all molecules have the same orientation [12].

Finally, it has been suggested that the molecules located in the vicinity of defects may behave differently from those composing a well-ordered planar hexagonal layer. Investigating the occurrence and the organization of defects in the structure of C_{60} layers is therefore of great interest for their possible applications.

It is also noteworthy that such investigations may have a more general impact, because planar hexagonal C_{60} layers may be considered as model objects for a wider class of two-dimensional molecular crystals. Indeed, the fullerene molecule has a closed-shell electronic structure due to the high strength of the chemical bonds between its carbon atoms. Thus, these bonds do not play a significant role in the formation of fullerene clusters. Further, the cohesive force between fullerenes are well understood [18]. In particular, an approximate potential for the interaction of two C_{60} molecules was proposed in [19].

In the present paper, we report a scanning tunneling microscopy (STM) study and a theoretical interpretation of a two-domain structure in C_{60} layers deposited onto WO_2/W(110) surfaces. The paper is organized as follows. Section II briefly describes the experimental technique and outlines the experimental observation of a polycrystalline structure with tilt boundaries in a two-dimensional fullerene layer. It is shown that the angular mismatch in the tilt boundary areas is accommodated by linear arrays of defected lattice patches, referred to as molecular structural units (MSUs). Section III presents a model of these rotational defects using an elastostatic field theory of crystal defects. It is shown that the MSUs can be interpreted in terms of a localized disclination dipole density field, whereas a dislocation interpretation renders unrealistic values for their energy. Conclusions are formulated in Sec. IV. The paper is completed with two Appendixes presenting some details of (A) the calculation of the absorption energy of a hexagonal network of C_{60} molecules over a nanorow WO_2/W substrate and (B) the theory of dislocation/disclination fields.

II. STM STUDY OF C$_{60}$ MONOLAYERS

The experiments were performed using a commercial STM from Createc, in an ultrahigh-vacuum (UHV) system consisting of an analysis chamber (with a base pressure of 2×10^{-11} mbar) and a preparation chamber (5×10^{-11} mbar). An electrochemically etched monocrystalline W(100) tip was used to record the images in constant current mode. The voltage V_t corresponds to the sample bias with respect to the tip. No drift corrections have been applied to any of the STM images presented in this paper. Details of the preparation of the WO$_2$/W(110) substrate surface and C$_{60}$ film deposition can be found elsewhere [10,20].

The WO$_2$/W(110) surface was found to exhibit a highly anisotropic nanorow pattern, as a result of a coincidence structure between the WO$_2$(010) monolayer and the W(110) surface [20]. In the STM images [Figs. 1(a) and 1(c)], the grooves and rows correspond to the largest and smallest mismatch between the atomic lattices of WO$_2$ and W(110), respectively. The periodic pattern of grooves and rows
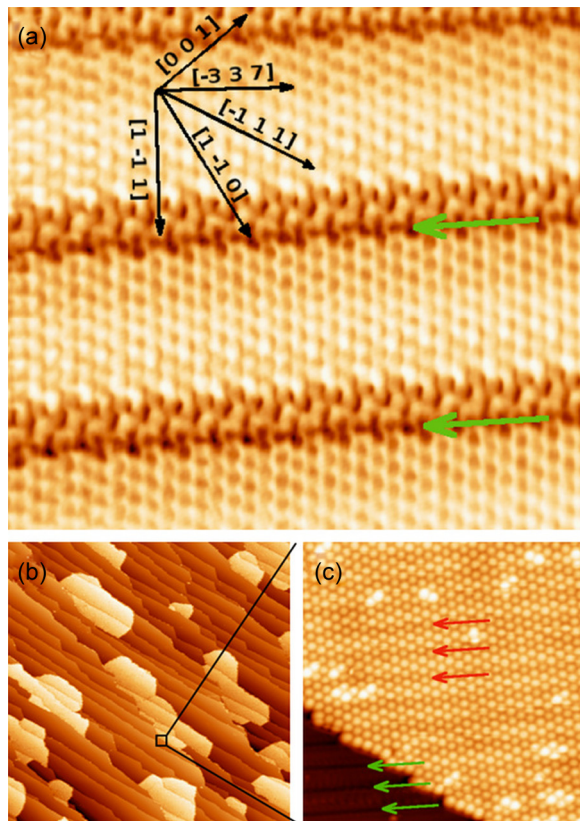

FIG. 1. (Color online) (a) 7.5×7.5 nm^2 STM image of WO$_2$/W(110) surface. The image was taken with a $V_b = +68$ mV sample bias voltage and $I_t = 100$ pA tunneling current. The crystallographic directions are indicated with respect to W(110). Green arrows indicate the positions of the grooves. (b) 400×400 nm^2 STM image of WO$_2$/W(110) surface covered by one-C$_{60}$-molecule-thick nano-islands. $V_b = 1.4$ V, $I_t = 34$ pA. (c) Magnified area demonstrating the connection of the C$_{60}$ film to terrace inner step edges. Green arrows indicate the periodic pattern of grooves on the WO$_2$/W(110) surface. Red arrows indicate grooves in the STM image of the C$_{60}$ film.
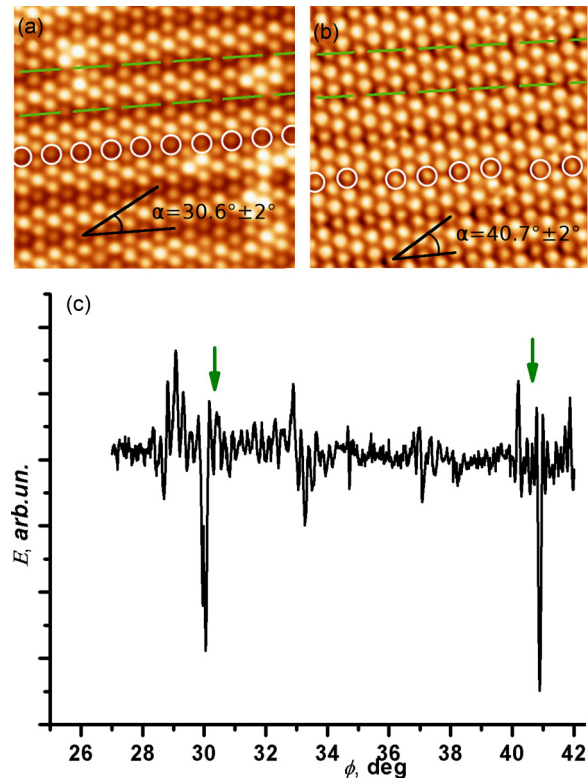

FIG. 2. (Color online) (a), (b) 16×16 nm^2 STM images of C$_{60}$ films of two preferred orientations. The grooves of WO$_2$/W(110) (indicated by green broken lines) appear in the STM images of the C$_{60}$ films as a periodic structure of dim molecules. One such a groove is highlighted by white circles. $V_b = 600$ mV, $I_t = 30$ pA, $T = 315$ K. (c) Calculated dependence of the absorption energy of 100×100 C$_{60}$ close-packed planar molecules cluster as a function of the angle between one of the close-packed directions of the film and the grooves direction. Green arrows indicate α, as measured from the STM experiment.

modulates properties of the surface in the direction normal to the rows [20].

The growth of the C$_{60}$ monolayer starts at terrace inner step edges [10] and forms C$_{60}$ islands [Fig. 1(b)] of close-packed hexagonal lattice with a molecule-molecule separation distance close to 1 nm [Figs. 1(c), 2(a), and 2(b)]. At certain voltage bias, the C$_{60}$ molecules on the WO$_2$/W(110) surface show a significant difference in apparent height [Figs. 2(a) and 2(b)], a reflection of local electronic and/or topographic variations. The grooves of WO$_2$/W(110) appear in the STM images of the C$_{60}$ films [indicated by red arrows in Fig. 1(c)] as a periodic linear array of dim molecules [marked by white circles in Figs. 2(a) and 2(b)]. The orientation α of the hexagonal lattice with respect to the direction of the rows of the WO$_2$/W(110) surface is $30.6° \pm 2°$ [Fig. 2(a)] in 80% of the C$_{60}$ islands. However, this orientation is different in about 20% of the C$_{60}$ islands, with α being equal to $40.7° \pm 2°$ [Fig. 2(b)]. This observation shows that the C$_{60}$-substrate interaction plays a significant role in the arrangement of the molecules in the layer. Indeed, the C$_{60}$ molecules are physisorbed on the WO$_2$/W(110) surface and the molecule-substrate interaction is determined by the van der Waals
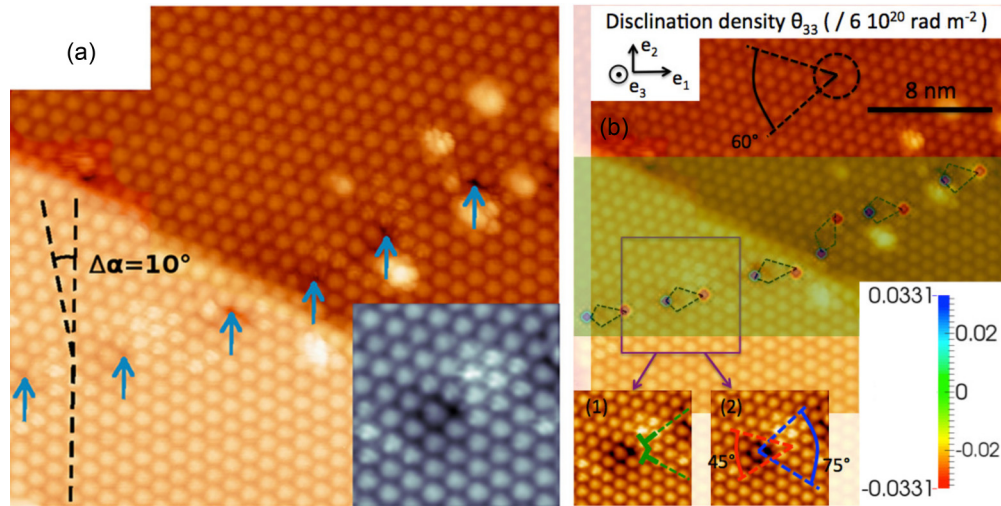
FIG. 3. (Color online) (a) STM image of a tilt boundary separating two differently oriented domains of the C$_{60}$ film. The misorientation of the domains is indicated by the angle $\Delta\alpha$ between two broken lines corresponding to the close-packed directions in the domains. The misorientation between the adjacent domains is realized by a linear array of molecular structural units, indicated by blue arrows. Black-and-white inset evidences orbital structure of squeezed C$_{60}$ molecules around the second MSU from the left. (b) Wedge-disclination density field superimposed on the bicrystal fullerene planar monolayer. The six MSUs along the tilt boundary are highlighted by dashed lines. Inset (1) shows the representation of one MSU with edge dislocations marked by two green lines. Inset (2) shows the measure of Frank vectors for the representation of the same MSU with a wedge-disclination dipole.

potential. Thus, the dependence of a C$_{60}$ molecule energy on its position across the rows must correlate with the variations of the electronic properties of the surface. By assuming from STM topography of the substrate that the absorption energy is piecewise homogeneous in grooves and rows and has higher value in grooves than in rows, the calculation of the total energy of a hexagonal network of 100×100 C$_{60}$ molecules deposited over a WO$_2$/W(110) surface, for varying orientation α (see Appendix A), showed that the network energy reaches minima for two values of α [Fig. 2(c)] equal to 40.9° and 30.2°, in good agreement with the observed values.

The existence of two preferred orientations results in tilt boundaries separating differently oriented domains [Figs. 3(a)] and in a planar polycrystalline structure of the C$_{60}$ monolayer. The tilt angle between the domains is $10° \pm 2°$, a value considered as small for grain boundaries in bulk solids. Close examination of the tilt boundary area in Fig. 3(a) reveals that the misorientation between adjacent domains is accommodated by a linear array of MSUs where rotational defects localize. In the MSUs, the hexagonal symmetry of the molecular lattice is broken: The elementary honeycomb pattern of the lattice is either opened by a positive wedge angle of value $+(15° \pm 2°)$ or constricted by a negative wedge angle $-(15° \pm 2°)$.

III. NATURE OF MSUs

We associate the MSUs with localized patches of continuous wedge-disclination density, with line and Frank vectors normal to the monolayer. Together with dislocations, disclinations were proposed by Volterra [21] to account for the discontinuity of elastic rotation and displacement along surfaces in a three-dimensional solid. In a virtual experiment, Volterra considered an elastic cylinder containing a line defect

(disclination or/and dislocation). The core of the defect along the cylinder axis is removed, and a cut along a half-plane terminating on the defect line is made. The cut induces rigid body motion of one edge of the cut with respect to the other. When this motion is a translation, the defect is referred to as a dislocation, whose strength is the (space-independent) translation vector known as the Burgers vector. A disclination is obtained when the motion is pure rotation. The strength of the disclination is the relative rotation vector of the undeformed edges of the cut, referred to as the Frank vector. The relative displacement of the edges in this rotation also gives rise to a space-dependent Burgers vector associated with the disclination. Disclinations have long been overlooked in the theory of crystal defects due to the large level of elastic energy they involve, as compared with dislocations, which precludes their occurrence as isolated objects. However self-screened configurations, such as disclination dipoles, involve relatively small elastic energy levels [22]. Disclination dipoles were recently shown to be pervasive along grain boundaries in metals of various crystallographic symmetries [23] and in mantle rocks [24]. They were also inferred from the observation of two-dimensional polycrystalline graphene [25].

In the present experiments, the disclination density patches shown in Fig. 3(b) are also spatially coupled in the form of dipoles superimposed on the MSUs, with a Frank vector magnitude of $\pm(15° + 2°)$. The framework of the theory used to interpret these results is presented in Refs. [26,27] and briefly described in Appendix B. By continuously specifying the displacement and rotation vector fields below intermolecular distances, the present interpretation considers the C$_{60}$ layer as capable of transmitting stresses and couple stresses at such a scale. The modeling paradigm thus consists in accounting for the lattice incompatibility arising from crystal defects (dislocations and disclinations) by focusing on the
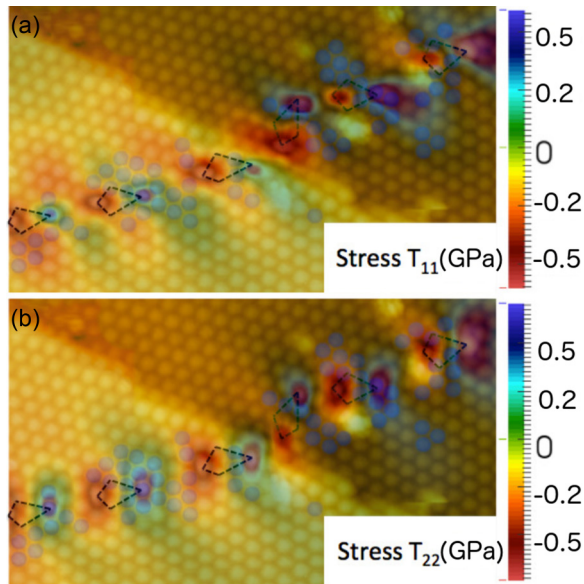
FIG. 4. (Color online) In-plane tensile stress fields superimposed on the bicrystal fullerene planar monolayer. Bright fullerenes displaying their orbital structure (blue spots) are seen to overlap with high-compression regions around negative disclinations.

defect densities, rather than on the molecules themselves [26]. The theory has the standard mathematical structure of a boundary value problem. The unknown fields are the tensorial defect densities and displacement vector fields, with standard boundary conditions on displacements and traction/moment vectors. As a consequence of this boundary value structure, approximate solutions for the fields of elastic displacement, rotation, strain, curvature, and energy over the layer can be generated using finite element methods [27].

In this aim, we used linear elastic laws for face-centered-cubic (fcc) lattices, showing hexagonal symmetry in their (111) plane, and elastic constants measured at room temperature in bulk fcc fullerene lattices [28]. The largest dilatation/contraction values predicted by the theory are localized at negative/positive disclination sites, respectively. They are of the order of 10%, in excellent agreement with the values measured by STM. Contractions tend to pull back the molecules to their equilibrium position in regions where the lattice opens, while dilatations tend to push them away from their equilibrium position where it is squeezed. The predicted tensile stress fields are shown in Figs. 4(a) and 4(b).

The comparison between the theoretical predictions and the experimental findings comes, in particular, through the rotational dynamics of the C_{60} molecules. At room temperature and sufficiently low pressure, the C_{60} molecules rotate freely [15]. This rotation smears their submolecular structure in STM images, where they appear as plain spheres. Instead, as can be seen in Fig. 3(a), molecules whose rotation is stopped display distinctly their electron orbital structure [15]. Remarkably, the areas where the orbital structure of the molecules is visible coincide with regions of high compressive stresses [Figs. 4(a) and 4(b)], amounting to 500 MPa, induced by the defected structure of the lattice around negative disclinations, which suggests that molecular rotation stops in these areas

due to pressure [29]. This conclusion is confirmed by our measurements of the average distance between molecules by STM. The latter is about 0.2 Å smaller between still molecules and their neighbors around negative disclinations than between freely rotating molecules, which results in a similar estimate of the overstress [30,31]. Most of the elastic energy of the defected areas is due to dilatations/contractions, although shear stresses are also present. The average energy density over the tilt boundary is 80 mJ/m^2, a rather small value as compared with the 1 J/m^2 energy density of symmetric tilt boundaries in bulk copper [32]. It is noteworthy that this value corresponds rather well with the estimates provided in [33] for the activation energy of deformation processes upon indentation.

The MSU defects can also be interpreted in terms of edge dislocations, with line vector normal to the layer and in-plane Burgers vector of length 1 nm. Indeed, pairs of additional half in-plane lines of C_{60} molecules terminating on the MSUs can be seen in Fig. 3(b). Since the tilt angle of the boundary is relatively small, it is tempting to disregard the disclination patterns and to look for an interpretation of the tilt boundary in terms of dislocations only, as customary in the case of low-angle boundaries in bulk solids. Such a pure dislocation model can also be worked out in the framework of our dislocation/disclination field theory. As a result, we found an average elastic energy density of 640 mJ/m^2 along the tilt boundary, a value much larger than in the disclination interpretation. Moreover, the compression stress field found from the pure dislocation theory reaches huge values of the order of 4 GPa and does not overlap the fullerenes with distinct orbital structure. The mismatch between these two interpretations originates in the form of the free energy [34]. In the sole presence of dislocations only the elastic strain enters the free energy. The solution is overly rigid to describe the nonuniformity of the energy field in the tilt boundary area. In the presence of disclinations, both elastic strains and curvatures are considered. The solution becomes more flexible and renders more precisely this distribution.

Therefore, we believe that the disclination model describes more adequately the tilt boundaries in the C_{60} monolayer. With proper calibration, the brightness of the fullerenes provides means to measure the height of the molecules with respect to the reference plane. We found deviations of the order of 0.2 Å in the MSUs, leading to elastic shear strain normal to the layer of about 10%. Such deviations suggest that the fullerene layer has actually a three-dimensional character in the defected regions and that our simple two-dimensional approximation may not be sufficient to describe consistently the core structure of the rotational defects. However, it makes it possible to describe accurately the pattern of MSUs within the tilt boundary and the elastic strain and energy density fields arising from the presence of defects in the fullerene layer.

IV. CONCLUSIONS

The STM study of the electronic surface properties of a C_{60} molecular layer deposited on a WO$_2$/W(110) substrate shows that a two-dimensional polycrystalline structure may arise in the layer in the presence of significant van der Waals interactions between substrate and layer. The

two-dimensional nanograins of the polycrystalline layer show a well-ordered hexagonal distribution of the molecules, due to their interactions, but with different energetically favorable orientations with respect to the substrate, which leads to tilt boundaries between the grains. In the tilt boundary areas, the STM images show that the angular incompatibility is accommodated by linear arrays of MSUs where the hexagonal symmetry of the molecular lattice is broken.

A theoretical approach is proposed to explain the nature of these defects in the hexagonal molecular lattice. It is based on an elastostatic field theory of crystal defects, where smoothness of the field variables is assumed at intermolecular distances. These variables include displacement, rotation, and crystal defect densities (dislocations and disclinations). Within this continuous framework, it is shown that the MSUs identified from the location of the molecules in the STM images can be interpreted in terms of localized disclination dipole density patches. The theory is then used to build maps of the elastic fields over the layer, including elastic strains, elastic dilation, and stresses.

The theoretical predictions are strongly corroborated by the observation of suppression of the rotation of the C$_{60}$ molecules in the regions of MSUs. Indeed, the STM images make it possible to tell the rotating molecules, seen as plain spheres, from the still molecules, where the details of the electronic structure become visible. It occurs that the areas where the electronic structure is distinctly seen overlap the high-compression regions around disclinations, as predicted by the theory.

ACKNOWLEDGMENTS

APPENDIX A: CALCULATION OF THE ABSORPTION ENERGY OF A HEXAGONAL NETWORK OF C$_{60}$ MOLECULES OVER A NANOROW WO$_2$/W SUBSTRATE

In the following, we develop a model based on STM observations to interpret the two preferred orientations of C$_{60}$ layers deposited on WO$_2$/W(110) surfaces, as shown in Figs. 2(a) and 2(b) of the main text. The idea outlined in the main text and presented below is that these two orientations correspond to cusps in the absorption energy vs orientation dependence.

The atomic structure of the WO$_2$/W(110) surface can be viewed as a coincidence structure between the WO$_2$(010) oxide layer and the W(110) surface [20]. The accommodation of incompatible elastic strains in areas of maximum lattice mismatch requires a dislocation network, resulting in a shift of the oxide layer by 0.1 nm in the [$\bar{3}$37] direction [see Fig. 1(a) in the main text]. Since the mismatch dislocations are aligned with the [$\bar{3}$37] direction, variations of the physical properties (including electronic properties) and some structuration can be expected in this direction. The STM images and cross
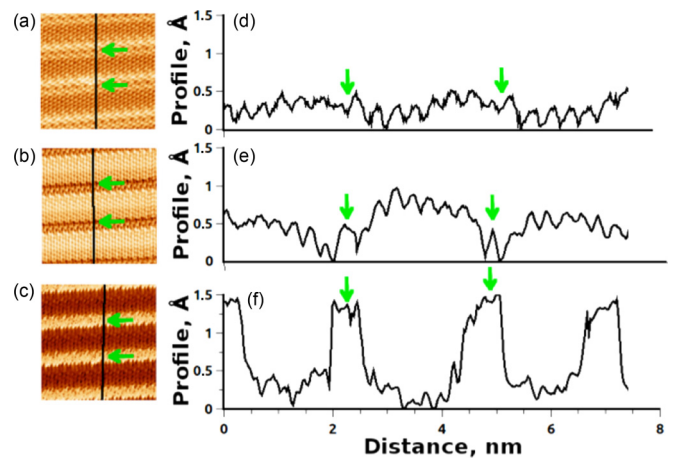

FIG. 5. (Color online) Evolution of 7.5×7.5 nm^2 STM images of the WO$_2$/W(110) surface (a)–(c) and corresponding cross sections (d)–(f) measured under different tunneling conditions: (a), (d) $V_b = -110$ mV, $I_t = 2.2$ nA; (b), (e) $V_b = 60$ mV, $I_t = 100$ pA; (c), (f) $V_b = -30$ mV, $I_t = 3$ nA. Green arrows indicate the groove positions.

sections presented in Fig. 5 demonstrate that deep grooves, indicated by green arrows in Figs. 5(b) and 5(e), transform into long-wavelength protrusions in Figs. 5(c) and 5(f), when the bias voltage V_b and tunneling current I_t are changed. The STM images shown in Figs. 5(a) and 5(d) also reveal much smaller short-wavelength oscillations in the groove areas, related to imaging of individual atoms. The long-wavelength pattern shows a dependence on the bias voltage V_b and tunneling current I_t, indicating that this modulation is due to variations of the local surface electronic properties. These observations are a clear evidence that the local surface electronic properties in a groove area are substantially different from those outside this area and that the long-wavelength dependence is associated with the periodic nanorow structure of the surface. In particular, the cross section shown in Fig. 5(f) clearly displays a meander-shaped, long-wavelength pattern. The latter is shown and schematized (red curve) in Fig. 6(a). Since the local absorption energy (LAE) of C$_{60}$ molecules over the WO$_2$/W(110) surface is determined by local electronic properties of the latter, one can reasonably infer from these observations that the LAE essentially depends on whether the absorption occurs in a groove area or not.

In the following model, we now propose to calculate the total absorption energy (TAE), as the sum of the LAEs of a hexagonal network of 100×100 C$_{60}$ molecules absorbed on a nanorow WO$_2$/W surface [Fig. 6(b)], as a function of the orientation angle α of the C$_{60}$ network with respect to the WO$_2$/W surface. The TAE is calculated for values of α ranging from 27° up to 42°. Following the discussion above, the LAE of a C$_{60}$ molecule is set either to 1 (arbitrary units) if its center of mass is located in a groove area or to 0 if not [see bottom panel of Fig. 6(a)]. The groove width is set to 0.7 nm, from measures on a set of STM images obtained under different (V_b, I_t) conditions. Figure 2(c) of the main text presents the absorption energy versus orientation curve predicted by the model. Two energy minima clearly stem from the curve for values of α equal to 40.9° and 30.2°. Hence, the two preferred
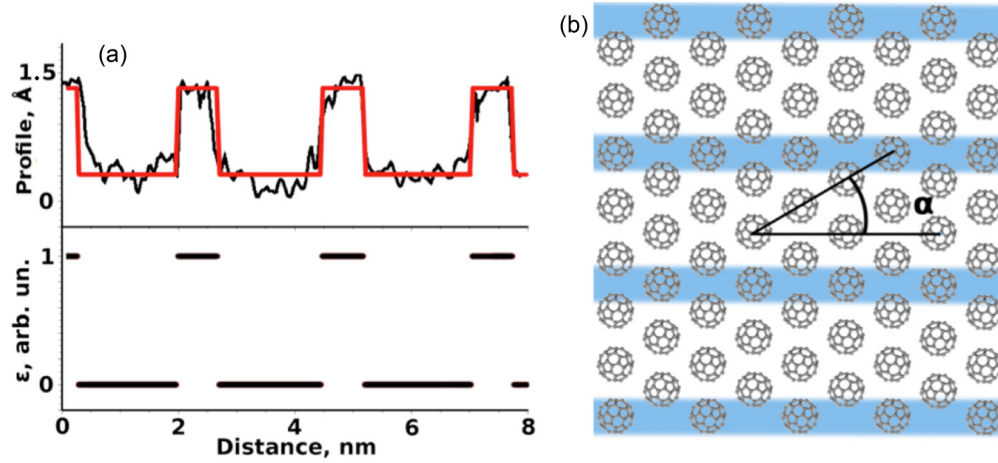
FIG. 6. (Color online) (a) Dependence of LAE of C_{60} molecules depending on their location on the periodic row structure. (Top) The black curve is a cross section of the STM image of the $WO_2/W(110)$ surface shown in Fig. 5(c); the red curve highlights the long, meander-shaped, wavelength component of the cross-section profile. (Bottom) LAE used in the present model. (b) Part of the hexagonal network of 100×100 C_{60} molecules used for the calculation of the TAE as a function of orientation angle α. The blue stripes represent the grooves.

orientations of the C_{60} films observed experimentally seem to correlate with the cusps in this energy curve, suggesting that the layer-substrate interactions play a significant role in the arrangement of C_{60} films.

APPENDIX B: ELASTOSTATIC THEORY OF DISCLINATION AND DISLOCATION FIELDS

The elastostatic part of the theory of disclination and dislocation fields [26] is briefly recalled. It is complemented with the derivation of a bidimensional model dedicated to C_{60} planar layers and with the construction of the field representation of a C_{60} film containing a tilt boundary.

1. Theoretical background

In a continuum mechanics setting in the absence of cracks, the displacement vector field **u** is defined continuously at any point of an elastoplastic body. The total distortion tensor, defined as the gradient of the displacement $\mathbf{U} = \mathbf{grad\,u}$, is curl free:

$$\mathbf{curl\,U} = 0. \tag{B1}$$

This equation is a necessary condition for the integrability of the displacement **u** and a compatibility condition for the distortion **U**. Conversely, it is sufficient to assure the existence of a single-valued continuous solution **u** to the equation $\mathbf{U} = \mathbf{grad\,u}$, up to a constant translation. In the presence of dislocations [35], the total distortion contains plastic, $\mathbf{U_p}$, and elastic, $\mathbf{U_e}$, parts, with incompatible, non-curl-free components, $\mathbf{U_p^\perp}$ and $\mathbf{U_e^\perp}$. Additional curl-free compatible components, $\mathbf{U_e^\parallel}$ and $\mathbf{U_p^\parallel}$, may be needed to satisfy the balance of equilibrium and boundary conditions. In the present paper, we are not interested in the dynamic process by which dislocations have been nucleated and transported into the body, and we can assume, without loss of generality, that $\mathbf{U_p^\parallel} = \mathbf{0}$.

The following relations are therefore satisfied:

$$\mathbf{U} = \mathbf{U_e} + \mathbf{U_p}, \tag{B2}$$

$$\mathbf{U_e} = \mathbf{U_e^\perp} + \mathbf{U_e^\parallel}, \tag{B3}$$

$$\mathbf{U_p} = \mathbf{U_p^\perp}, \tag{B4}$$

$$0 = \mathbf{U_e^\perp} + \mathbf{U_p^\perp}, \tag{B5}$$

$$\mathbf{curl\,U_e^\perp} = -\mathbf{curl\,U_p^\perp} = \boldsymbol{\alpha} \neq 0. \tag{B6}$$

Equations (B6) are satisfied by the incompatible plastic distortion $\mathbf{U_p^\perp}$ associated with the presence of Nye's dislocation density tensor $\boldsymbol{\alpha}$ [36] and by the incompatible elastic distortion $\mathbf{U_e^\perp}$ offsetting the latter and ensuring the continuity of matter implied by Eq. (B1). Since $\mathbf{U_e^\parallel}$ is curl free, Eqs. (B6) also implied

$$\mathbf{curl\,U_e} = \boldsymbol{\alpha}. \tag{B7}$$

By decomposing the elastic distortion into its symmetric and skew-symmetric parts, Eq. (B7) can alternatively be expressed as [22,26]

$$\mathbf{curl\,}\boldsymbol{\epsilon}_e = \boldsymbol{\alpha} + \boldsymbol{\kappa}_e^t - tr(\boldsymbol{\kappa}_e)\mathbf{I}. \tag{B8}$$

Equation (B8) relates the incompatibility in elastic strain $\boldsymbol{\epsilon}_e$ arising from the presence of Nye's dislocation density tensor $\boldsymbol{\alpha}$, and the elastic, $\boldsymbol{\kappa}_e$ curvature. In the elastic theory of dislocations, the elastic and total, $\boldsymbol{\kappa}$, curvature tensors write

$$\boldsymbol{\kappa}_e = \boldsymbol{\kappa} = \mathbf{grad\,}\vec{\omega}_e = \mathbf{grad\,}\vec{\omega}. \tag{B9}$$

The elastic curvature is curl free and the associated rotation vector $\vec{\omega}_e = \vec{\omega} = \frac{1}{2}\mathbf{curl\,u}$ is an integrable single-valued quantity. As shown by deWit [22], $\boldsymbol{\kappa}_e$ may not be curl free anymore if the possibility of multivalued elastic and plastic rotations $\vec{\omega}_e$ and $\vec{\omega}_p$, i.e., a discontinuity of the elastic and plastic rotations over some surface, is acknowledged. In such a situation, a nonzero tensor $\boldsymbol{\theta}$ such that

$$\boldsymbol{\theta} = -\mathbf{curl\,}\boldsymbol{\kappa}_p = \mathbf{curl\,}\boldsymbol{\kappa}_e \tag{B10}$$

can be defined. $\boldsymbol{\theta}$ is the polar disclination density tensor [22], while $\boldsymbol{\kappa}_p$ is the plastic curvature tensor. Again, the elastic and

plastic curvature tensors have incompatible parts, $(\boldsymbol{\kappa}_e{}^\perp, \boldsymbol{\kappa}_p{}^\perp)$, and compatible (curl-free) parts $(\boldsymbol{\kappa}_e{}^\parallel, \boldsymbol{\kappa}_p{}^\parallel)$, but we are not interested in the dynamic process by which the disclinations have been nucleated and transported in the body. Hence, we may assume $\boldsymbol{\kappa}_p{}^\parallel = 0$ without loss of generality, and relations similar to Eqs. (B2)–(B5) are satisfied by the curvatures. The discontinuity of the elastic rotation resulting from the presence of disclinations is referred to as the Frank vector. It is obtained by integrating the incompatible elastic curvatures along a closed circuit C:

$$\boldsymbol{\Omega} = \int_C \boldsymbol{\kappa}_e{}^\perp \cdot \mathbf{dr} = \int_C \boldsymbol{\kappa}_e \cdot \mathbf{dr}. \tag{B11}$$

Similarly, the discontinuity of the elastic displacement is the Burgers vector. It contains a possible contribution from the nonuniformity of elastic curvatures and reads [22]

$$\mathbf{b} = \int_C \left[\boldsymbol{\epsilon}_e - \left(\boldsymbol{\kappa}_e^t \times \mathbf{r} \right)^t \right] \cdot \mathbf{dr}. \tag{B12}$$

If S is the surface of unit normal $\mathbf{n}$ delimited by the circuit C, using Stokes's theorem and Eqs. (B8) and (B10) allows rewriting Eqs. (B11) and (B12) as

$$\boldsymbol{\Omega} = \int_S \boldsymbol{\theta} \cdot \mathbf{n} dS, \tag{B13}$$

$$\mathbf{b} = \int_S [\boldsymbol{\alpha} - (\boldsymbol{\theta}^t \times \mathbf{r})^t] \cdot \mathbf{n} dS. \tag{B14}$$

$\boldsymbol{\Omega}$ and $\mathbf{b}$ defined above are pointwise measures of the lattice incompatibility in the presence of disclinations and dislocations. In contrast, the disclination and dislocation densities $\boldsymbol{\theta}$ and $\boldsymbol{\alpha}$ defined in Eqs. (B8) and (B10) are continuous tensorial renditions of this incompatibility. They provide a natural regularization of the singular and discontinuous nature of the Frank/Burgers vectors.

In the absence of inertia and body forces, the momentum and moment of momentum equation reduce to [37,38]

$$\mathbf{div}\, \mathbf{T}^{\text{sym}} + \tfrac{1}{2} \mathbf{curl}\, \mathbf{div}\, \mathbf{M}^{\text{dev}} = 0. \tag{B15}$$

In the above, $\mathbf{T}^{\text{sym}}$ and $\mathbf{M}^{\text{dev}}$ denote the symmetric Cauchy stress tensor and the deviatoric part of the couple stress tensor, respectively. A specific free-energy density function ψ containing contributions from elastic strains and curvatures is now introduced as follows:

$$\psi = \psi(\boldsymbol{\epsilon}_e, \boldsymbol{\kappa}_e). \tag{B16}$$

Following recent developments [34], the elastic constitutive relations for $\mathbf{T}^{\text{sym}}$ and $\mathbf{M}^{\text{dev}}$ are chosen in the linear form:

$$\mathbf{T}^{\text{sym}} = \mathbf{C} : \boldsymbol{\epsilon}_e + \mathbf{D} : \boldsymbol{\kappa}_e, \tag{B17}$$

$$\mathbf{M}^{\text{dev}} = \mathbf{A} : \boldsymbol{\kappa}_e + \mathbf{B} : \boldsymbol{\epsilon}_e. \tag{B18}$$

A determination of the tensors of elastic constants $\mathbf{A}$, $\mathbf{B}$, $\mathbf{C}$, and $\mathbf{D}$ is provided in the framework of a bidimensional model dedicated to C$_{60}$ planar layers in the next section.

2. Two-dimensional edge-dislocation wedge-disclination model

The two-dimensional elastic edge-dislocation wedge-disclination model [24,38] is now briefly recalled for completeness. The model describes the elastic strain and stress fields

arising from the presence of crystal defects and the application of loads on a two-dimensional medium as a special case of the full three-dimensional theory of crystal defects presented above. We limit the fields of crystal defects envisioned to distributions of wedge disclinations and edge dislocations with line normal to the plane $(\mathbf{e_1}, \mathbf{e_2})$ in the orthonormal reference frame $(\mathbf{e_1}, \mathbf{e_2}, \mathbf{e_3})$, which is sufficient for the description of the C$_{60}$ planar layer containing a tilt boundary. Thus, we assume the disclination tensor $\boldsymbol{\theta} = \theta_{33} \mathbf{e_3} \otimes \mathbf{e_3}$, all other components being zero. θ_{33} depends only on the coordinates (x_1, x_2). The incompatibility equation (B10) defining the disclination density tensor reduces to

$$\theta_{33} = \kappa_{32,1}^e - \kappa_{31,2}^e. \tag{B19}$$

Hence, the only relevant elastic curvatures are $(\kappa_{31}^e, \kappa_{32}^e)$. In a plane strain setting, the components of the elastic strain tensor are $(\epsilon_{11}^e, \epsilon_{12}^e, \epsilon_{21}^e, \epsilon_{22}^e)$. From Eq. (B8), the dislocation density tensor $\boldsymbol{\alpha}$ is defined from the curl of the elastic strains and the curvatures, which yields the edge components

$$\alpha_{13} = -\epsilon_{11,2}^e + \epsilon_{12,1}^e - \kappa_{31}^e, \tag{B20}$$

$$\alpha_{23} = -\epsilon_{21,2}^e + \epsilon_{22,1}^e - \kappa_{32}^e. \tag{B21}$$

The balance of momentum and moment of momentum equation (B15) reduces to

$$T_{11,1}^{\text{sym}} + T_{12,2}^{\text{sym}} + \tfrac{1}{2}(M_{31,1} + M_{32,2})_{,2} = 0, \tag{B22}$$

$$T_{21,1}^{\text{sym}} + T_{22,2}^{\text{sym}} - \tfrac{1}{2}(M_{31,1} + M_{32,2})_{,1} = 0. \tag{B23}$$

We now describe the elastic properties of the defected two-dimensional lattice, with particular focus on the core region of the defects. The discussion is limited to the present edge-wedge dislocations/disclinations. As mentioned in the main text, we assume fcc symmetry of a virtual bulk C$_{60}$ molecular lattice whose (111) plane, which features hexagonal symmetry, is the actual present two-dimensional C$_{60}$ lattice. Hence, the relations $C_{1111} = C_{2222}, C_{1122} = C_{2211}, C_{1221} = C_{1212} = C_{2112} = C_{2121}$ hold between the components of the elastic tensor $\mathbf{C}$. The values used in the present work are taken at room temperature from the work [28]: $C_{1111} = 15\,\text{GPa}, C_{1222} = 9\,\text{GPa}, C_{1212} = 7\,\text{GPa}$. The dimensions of the elastic constants in tensors $\mathbf{A}$ and $(\mathbf{B}, \mathbf{D})$ are respectively that of stress $\times$ length^2 and stress $\times$ length. The elastic tensor $\mathbf{A}$ induces couple stresses in the defected regions of the lattice, because the symmetry of the stress tensor is broken by the fluctuations of the molecular interactions. Both $\mathbf{B}$ and $\mathbf{D}$ are zero in isotropic, centrosymmetric media. However, centrosymmetry is broken in the presence of defects, which yields nonzero $\mathbf{B}$ and $\mathbf{D}$ tensors in the defected areas [34]. Due to tensor $\mathbf{D}$, the strong fluctuations of the elastic rotation over the defect core region induce stresses, whereas the tensor $\mathbf{B}$ gives rise to couple stresses following from the fluctuations in lattice strain. As detailed in [24,38], the symmetric stress tensor takes the form

$$T_{11}^{\text{sym}} = C_{1111} \epsilon_{11}^e + C_{1122} \epsilon_{22}^e - D_{1131} \kappa_{31}^e + D_{1132} \kappa_{32}^e, \tag{B24}$$

$$T_{12}^{\text{sym}} = C_{1212} \epsilon_{12}^e + C_{1221} \epsilon_{21}^e + D_{1231} \kappa_{31}^e - D_{1232} \kappa_{32}^e, \tag{B25}$$

$$T_{21}^{\text{sym}} = C_{2112}\epsilon_{12}^e + C_{2121}\epsilon_{21}^e + D_{2131}\kappa_{31}^e - D_{2132}\kappa_{32}^e, \tag{B26}$$

$$T_{22}^{\text{sym}} = C_{2211}\epsilon_{11}^e + C_{2222}\epsilon_{22}^e + D_{2232}\kappa_{32}^e - D_{2231}\kappa_{31}^e. \tag{B27}$$

The couple-stress components (M_{31}, M_{32}) take the form

$$M_{31} = A_{3131}\kappa_{31}^e - B_{3111}\epsilon_{11}^e + B_{3112}\epsilon_{12}^e + B_{3121}\epsilon_{21}^e, \tag{B28}$$

$$M_{32} = A_{3232}\kappa_{32}^e - B_{3212}\epsilon_{12}^e - B_{3221}\epsilon_{21}^e + B_{3222}\epsilon_{22}^e. \tag{B29}$$

The **B** and **D** tensors characterize nonlocal elastic behavior in the defected crystal. From the results of Upadhyay *et al.* [34], the symmetry $B_{ijkl} = D_{klij}$ of the elastic constants holds. Further, we make the simplest possible choice for the nonzero components of the elasticity tensors **A**,**B**,**D**: $A_{ijkl} = \mu r^2$, $B_{ijkl} = D_{klij} = \mu r$, with $\mu = C_{1212} = 7$ GPa. The distance r is an internal length scale that sets the characteristic dimension of the area over which inhomogeneity of the elastic curvatures/strains induces a significant stress/couple stress component. Here we pick out the value $r = 0.5$ nm from Fig. 3 to limit this area to the core region of the defects.

3. Building the field representation of the molecular structure of the C_{60} tilt boundary

As outlined in the main text, the focus in the theory is on crystal defect density fields rather than on the molecules themselves. In the present planar model, an input for the simulation of the C_{60} tilt boundary shown in Fig. 3 by the finite element method [39] is the θ_{33} wedge-disclination density field. In what follows, we construct the disclination rendering of the C_{60} tilt boundary from the analysis of the molecular patterns. The construction follows that used in olivine tilt boundaries [24]. Far away from the boundary, the hexagonal

molecular honeycomb structure delineated by a black dotted circle in the figure is the constitutive element of regions whose elastic energy is minimum, to be used as a reference for the characterization of the disclinations. Each elementary structure is composed of a central C_{60} molecule, surrounded by six other molecules forming a symmetric hexagon, with a characteristic $60°$ angle. Six MSUs composing the tilt boundary structure can be identified in the figure. As shown in the inset (2), these MSUs are made of pairs of defected hexagonal patterns located at their tips. These patterns are elementary hexagonal structures whose hexagonal symmetry is broken. Locally, the angular distance between two C_{60} molecules is either increased from the reference $60°$ angle up to $75° \pm 2°$ at the left tip of the MSUs, or decreased down to $45° \pm 2°$ at their right tip. Such rotational defects are the signature of wedge disclinations. In the reference frame shown in Fig. 3, the wedge-disclination lines lay along the $\mathbf{e}_3$ axis and their wedge angles, i.e., the rotational defect of the unsymmetrical patterns, is measured around the $\mathbf{e}_3$ axis. Thus, each MSU corresponds to a dipole of θ_{33} wedge-disclination density patches. At the left tip of the MSU, a positive wedge-disclination density patch of Frank vector magnitude $+15° \pm 2°$ opens the molecular lattice from the $60°$ reference angle to $75° \pm 2°$. Conversely, at the right tip, a negative wedge-disclination density spot of Frank vector magnitude $-15° \pm 2°$ closes the lattice from the $60°$ reference down to $45° \pm 2°$. The wedge-disclination density field thus identified is superimposed on the molecular structure of the C_{60} tilt boundary in Fig. 3 and is used as an initial condition for the finite element simulation of the C_{60} boundary. In the boundary area, the finite element characteristic size is 0.25 nm, lower than intermolecular distances, to account for the details of its structure. The sample is made sufficiently large to ensure that applying zero traction and moment conditions on its external boundaries does not affect the elastic stress field of the disclination dipoles.

[1] Klaus D. Sattler (ed.), *Handbook of Nanophysics: Clusters and Fullerenes* (CRC Press, Taylor & Francis Group, Boca Raton, London, New York, 2011).

[2] D. Bonifazi, O. Enger, and F. Diederich, Chem. Soc. Rev. **36**, 390 (2007).

[3] E. Xenogiannopoulou, M. Medved, K. Iliopoulos, S. Couris, M. G. Papadopoulos, D. Bonifazi, C. Sooambar, A. Mateo-Alonso, and M. Prato, Chem. Phys. Chem. **8**, 1056 (2007).

[4] S. J. van der Molen and P. Liljeroth, J. Phys.: Condens. Matter **22**, 133001 (2010).

[5] H. Park, J. Park, A. K. L. Lim, E. H. Anderson, A. P. Alivisatos, and P. L. McEuen, Nature (London) **407**, 57 (2000).

[6] A. F. Hebard, M. J. Rosseinsky, R. C. Haddon, D. W. Murphy, S. H. Glarum, T. T. M. Palstra, A. P. Ramirez, and A. R. Kortan, Nature (London) **350**, 600 (1991).

[7] K. Tanigaki, T. W. Ebbesen, S. Saito, J. Mizuki, J. S. Tsai, Y. Kubo, and S. Kuroshima, Nature (London) **352**, 222 (1991).

[8] H. I. Li, K. J. Franke, J. I. Pascual, L. W. Bruch, and R. D. Diehl, Phys. Rev. B **80**, 085415 (2009).

[9] R. Z. Bakhtizin, T. Hashizume, Sh. Wang, and T. Sakurai, Phys. Usp. **40**, 275 (1997).

[10] S. Krasnikov, S. Bozhko, K. Radican, O. Lübben, B. Murphy, S. R. Vadapoo, H. C. Wu, M. Abid, V. Semenov, and I. Shvets, Nano Res. **4**, 194 (2011).

[11] F. Loske, R. Bechstein, J. Schtte, F. Ostendorf, M. Reichling, and A. Khnle, Nanotechnology **20**, 065606 (2009).

[12] J. G. Hou, Yang Jinlong, Wang Haiqian, Li Qunxiang, Zeng Changgan, Yuan Lanfeng, Wang Bing, D. M. Chen, and Zhu Qingshi, Nature (London) **409**, 304 (2001).

[13] D. V. Gruznev, A. V. Matetskiy, L. V. Bondarenko, A. V. Zotov, A. A. Saranin, J. P. Chou, C. M. Wei, and Y. L. Wang, Surf. Sci. **612**, 31 (2013).

[14] K. Aït-Mansour, P. Ruffieux, W. Xiao, P. Gröning, R. Fasel, and O. Gröning, Phys. Rev. B **74**, 195418 (2006).

[15] S. I. Bozhko, S. A. Krasnikov, O. Lübben, B. E. Murphy, K. Radican, V. N. Semenov, H. C. Wu, B. Bulfin, and I. V. Shvets, Phys. Rev. B **84**, 195412 (2011).

[16] J. A. Gardener, G. A. D. Briggs, and M. R. Castell, Phys. Rev. B **80**, 235434 (2009).

[17] K. O. Graivoronska, M. Klimenkov, Yu. M. Solonin, S. A. Nepijko, and G. Schönhense, Cryst. Res. Technol. **47**, 1255 (2012).

[18] M. Nakamura, *Handbook of Nanophysics: Clusters and Fullerenes*, edited by Klaus D. Sattler (CRC Press, Taylor & Francis Group, Boca Raton, London, New York, 2011), p. 37.

[19] L. A. Girifalco, J. Phys. Chem. **95**, 5370 (1991); **96**, 858 (1992).

[20] K. Radican, S. Bozhko, S.-R. Vadapoo, S. Ulucan, H.-C. Wu, A. McCoy, and I. Shvets, Surf. Sci. **604**, 1548 (2010).

[21] V. Volterra, Ann. Sci. Ecole Norm. Sup. **24**, 401 (1907).

[22] R. deWit, J. Res. Natl. Bur. Stand., Sect. A **77A**, 607 (1973).

[23] B. Beausir and C. Fressengeas, Int. J. Solids Struct. **50**, 137 (2013).

[24] P. Cordier, S. Demouchy, B. Beausir, V. Taupin, F. Barou, and C. Fressengeas, Nature (London) **507**, 51 (2014).

[25] J. Wu and Y. Wei, J. Mech. Phys. Solids **61**, 1421 (2013).

[26] C. Fressengeas, V. Taupin, and L. Capolungo, Int. J. Solids Struct. **48**, 3499 (2011).

[27] S. Varadhan, A. J. Beaudoin, A. Acharya, and C. Fressengeas, Model. Simul. Mater. Sci. Eng. **14**, 1245 (2006).

[28] N. P. Kobelev, R. K. Nikolaev, N. S. Sidorov, and Ya. M. Soifer, Phys. Solid State **43**, 2262 (2001).

[29] O. Andersson, A. Soldatov, and B. Sundqvist, Phys. Rev. B **54**, 3093 (1996).

[30] A. Lundin and B. Sundqvist, Phys. Rev. B **53**, 8329 (1996).

[31] K. P. Bohnen and R. Heid, Phys. Rev. Lett. **83**, 1167 (1999).

[32] V. Taupin, L. Capolungo, C. Fressengeas, A. Das, and M. Upadhyay, J. Mech. Phys. Solids **61**, 370 (2013).

[33] V. S. Bobrov, R. A. Dilanyan, L. S. Fomenko, Yu. L. Iunin, M. A. Lebyodkin, S. V. Lubenets, V. I. Orlov, and Yu. A. Ossipyan, J. Supercond. **8**, 1 (1995).

[34] M. Upadhyay, L. Capolungo, V. Taupin, and C. Fressengeas, Philos. Mag. **93**, 794 (2013).

[35] A. Acharya, J. Mech. Phys. Solids **49**, 761 (2001).

[36] J. F. Nye, Acta Metall. **1**, 153 (1953).

[37] R. D. Mindlin and H. F. Tiersten, Arch. Ration. Mech. Anal. **11**, 415 (1962).

[38] V. Taupin, L. Capolungo, and C. Fressengeas, Int. J. Plast. **53**, 179 (2014).

[39] F. Hecht, O. Pironneau, A. Le Hyaric, and K. Ohtsuka, FREEFEM++, www.freefem.org/ff++/